Characterization of structural and functional domains of the anillin-related protein Mid1p that contribute to cytokinesis in fission yeast

Shambaditya Saha[a] and Thomas D. Pollard[a,b]
[a]Department of Molecular Biophysics and Biochemistry and [b]Departments of Molecular, Cellular and Developmental Biology and of Cell Biology, Yale University, New Haven, CT 06520-8103

ABSTRACT **Fission yeast cells depend on the anillin-related protein Mid1p for reliable cytokinesis. Insolubility limits the purification of full-length Mid1p for biophysical analysis, and lack of knowledge about the structural domains of Mid1p limits functional analysis. We addressed these limitations by identifying in a bacterial expression screen of random Mid1p fragments five soluble segments that can be purified and one insoluble segment. Using complementation experiments in Δ*mid1* cells, we tested the biological functions of these six putative domains that account for full-length Mid1p. The N-terminal domain (residues 1–149) is essential for correct positioning and orientation of septa. The third domain (residues 309–452) allows the construct composed of the first three domains (residues 1-452) to form hydrodynamically well-behaved octamers. Constructs consisting of residues 1–452 or 1–578 carry out most functions of full-length Mid1p, including concentration at the equatorial cortex in nodes that accumulate myosin-II and other contractile ring proteins during mitosis. However, cells depending on these constructs without the insoluble domain (residues 579–797) form equatorially located rings slowly from strands rather than by direct condensation of nodes. We conclude that residues 1–578 assemble node components myosin-II, Rng2p, and Cdc15p, and the insoluble domain facilitates the normal, efficient condensation of nodes into rings.**

Monitoring Editor
Yu-Li Wang
Carnegie Mellon University

Received: Jun 14, 2012
Revised: Aug 14, 2012
Accepted: Aug 14, 2012

INTRODUCTION

The fission yeast, *Schizosaccharomyces pombe*, divides by medial fission dependent on a contractile ring of actin filaments and myosin-II (Pollard and Wu, 2010). Cells prepare for cytokinesis early in interphase by accumulating proteins in multiple punctate cortical structures called nodes. These interphase nodes contain the kinases Cdr2p, Cdr1p, and Wee1p, putative RhoGEF Gef2p, kinesin-like protein Klp8p, and uncharacterized protein Blt1p (Morrell *et al.*, 2004; Martin and Berthelot-Grosjean, 2009; Moseley *et al.*, 2009). Late in interphase the anillin-related protein Mid1p begins to move from the nucleus to interphase nodes at the cell equator (Paoletti and Chang, 2000; Moseley *et al.*, 2009). As cells enter mitosis, interphase nodes mature into cytokinetic nodes by recruiting contractile ring proteins through two parallel pathways: Mid1p recruits IQGAP protein Rng2p and conventional myosin-II (hereafter called Myo2, consisting of heavy chain Myo2p and light chains Cdc4p and Rlc1p); and Mid1p recruits F-BAR protein Cdc15p (Wu *et al.*, 2003, 2006; Almonacid *et al.*, 2011; Laporte *et al.*, 2011; Padmanabhan *et al.*, 2011). Both pathways help to recruit formin Cdc12p to nodes (Laporte *et al.*, 2011). Cdc12p then generates actin filaments that interact with Myo2 in adjacent nodes as the nodes condense into a contractile ring (Kovar *et al.*, 2003; Vavylonis *et al.*, 2008).

Cytokinesis is unreliable in cells without Mid1p. One-third of cells fail to assemble contractile rings (see accompanying article, Saha and Pollard, 2012) and contractile rings are misplaced or oriented obliquely in many other cells (Sohrmann *et al.*, 1996; Paoletti and

This article was published online ahead of print in MBoC in Press (http://www.molbiolcell.org/cgi/doi/10.1091/mbc.E12-07-0536) on August 23, 2012.

Address correspondence to: Thomas D. Pollard (thomas.pollard@yale.edu).

Abbreviations used: CD, circular dichroism; DIC, differential interference contrast; DTT, dithiothreitol; EDTA, ethylenediaminetetraacetic acid; GEF, guanine nucleotide exchange factor; GFP, green fluorescent protein; IPTG, isopropyl-β-D-1-thiogalactopyranoside; IQGAP, IQ motif containing GTPase activating protein; LB, Luria-Bertani (bacterial culture medium); mEGFP, monomeric enhanced green fluorescent protein; NES, nuclear export sequence; Ni-NTA, nickel–nitrilotriacetic acid; PH, pleckstrin homology; SD, standard deviation; TCEP, Tris(2-carboxyethyl) phosphine hydrochloride.

Chang, 2000). Cells lacking Mid1p or expressing Mid1p mutants assemble contractile rings from strands of actin filaments and Myo2 (Chang *et al.*, 1996; Paoletti and Chang, 2000; Sohrmann *et al.*, 1996; Motegi *et al.*, 2004; Hachet and Simanis, 2008; Huang *et al.*, 2008). The accompanying article (Saha and Pollard, 2012) shows that without Mid1p, cytokinetic nodes are scattered in the cortex, where they accumulate formin Cdc12p but not Myo2, Rng2p, or Cdc15p. Actin filaments produced by Cdc12p attract myosin-II into strands dispersed throughout the cortex that slowly merge into a contractile ring.

Analysis of Mid1p constructs with deletions or point mutations mapped regions of the protein important for intracellular localization, interactions with other cytokinesis proteins (Paoletti and Chang, 2000; Celton-Morizur *et al.*, 2004; Clifford *et al.*, 2008; Almonacid *et al.*, 2009, 2011; Lee and Wu, 2012; Ye *et al.*, 2012), and assembly of oligomers (Celton-Morizur *et al.*, 2004). However, many questions remained about the contributions of the various parts of Mid1p to cytokinesis. Sequence analysis revealed only the C-terminal pleckstrin homology (PH) domain (Sohrmann *et al.*, 1996), leaving open questions about the boundaries of any independently folded domains in the large (920 residues) Mid1p protein and number of subunits in the native protein, information required to understand the interactions of Mid1p that contribute to cytokinesis.

Challenges in purifying the largely insoluble Mid1p have limited biophysical studies, so we took the alternate strategy of identifying and characterizing soluble parts of Mid1p. We used a bacterial expression screen to identify five soluble segments of the protein and one large insoluble segment that account for the entire length of Mid1p. We refer to these segments as putative domains, pending further structural studies. Knowledge of the structural domains of Mid1p is equally valuable for functional studies because mutations and deletions that result in loss of functions are less likely to be artifacts when based on structural domains rather than arbitrary pieces of such a large protein.

RESULTS

Five soluble domains and one insoluble domain account for entire length of Mid1p

We used a bacterial expression screen to identify soluble regions of the large, insoluble Mid1p. Our screen was inspired by two previous studies (Kawasaki and Inagaki, 2001; Jacobs *et al.*, 2005) and based on the observation by Waldo *et al.* (1999) that the fluorescence of bacteria expressing polypeptides fused upstream of GFP correlates with the solubility of the fused polypeptide. We used this strategy to identify random pieces of Mid1p that expressed well in bacteria when fused to the N-terminus of monomeric enhanced green fluorescent protein (mEGFP). We used tagged random primer PCR (Grothues *et al.*, 1993) to construct a library of fragments of the coding sequence of Mid1p. We cloned fragments of 200 base pairs to 2.8 kb (full-length Mid1) in a plasmid vector upstream of mEGFP and transformed *Escherichia coli* cells with the plasmid library. We selected transformed cells by growth on Luria-Bertani (LB) plates containing ampicillin and identified brightly fluorescent colonies expressing Mid1p polypeptides fused upstream of mEGFP (Figure 1, A and B).

We sequenced cDNA inserts from fluorescent colonies to identify expressed Mid1p fragments (Figure 1C). Some bright colonies were false positives and expressed only mEGFP without any upstream Mid1p fragment. Plasmids from some colonies with low or no fluorescence contained fragments of Mid1 cDNA in-frame with mEGFP, whereas others were out of frame with mEGFP. We constructed and screened additional fragment libraries from regions of Mid1 cDNA underrepresented in initial rounds of screening.

Our screen of ~27,600 colonies through five rounds (Supplemental Table S1) yielded 16 highly expressed fragments of Mid1p (Figure 1C), which we used to define the approximate boundaries of six putative domains: M1-1 (residues 1–149), M1-2 (150–308), M1-3 (309–452), M1-4 (453–578), M1-5 (579–797), and M1-6 (798–920). The location of M1-5 was inferred from the lack of soluble fragments including residues 579–797. The DomPred Protein Domain Prediction Server (Marsden *et al.*, 2002) predicted the boundaries between M1-2 and M1-3 and between M1-5 and the C-terminal PH domain (Figure 1C, filled bars).

Physical properties of Mid1p constructs

Mid1p fragments M1-1, M1-2, M1-3, M1-4, and M1-6 were soluble when expressed in *E. coli*, but fragment M1-5 was insoluble (Figure 1D). We purified the soluble fragments of Mid1p and combinations of fragments (M1-12, M1-13, M1-14, and M1-124) using for each an optimized combination of nickel-nitriloacetic acid (Ni-NTA) affinity, ion-exchange, and size-exclusion chromatography. Mid1p domains M1-4 and M1-6 contain tryptophan, so we used differences in intrinsic tryptophan fluorescence emission spectra ±5.6 M urea to show that both had tertiary structure (Supplemental Figure S1, A and B).

Sedimentation velocity analytical ultracentrifugation showed that domain M1-3 allows Mid1p to form hydrodynamically well behaved oligomers (Figure 2, A–C). Both constructs M1-12 (consisting of domains M1-1 and M1-2) and M1-13 (consisting of domains M1-1 through M1-3) were homogeneous (Figure 2, A and B), and their sedimentation coefficients were independent of concentration over a 7- to 10-fold range, extrapolating to $S_{20,w}$ values of 2.1 S for M1-12 and 14.6 S for M1-13 (Figure 2C). We measured diffusion coefficients (D) from boundary spreading of the homogeneously sedimenting species and by size-exclusion chromatography (Table 1). The values of D from the two methods agreed for the range of concentrations of M1-12 but differed for the lowest concentration of M1-13, likely due to low signal-to-noise ratio (Supplemental Table S2) rather than dissociation of the oligomer, because the sedimentation was independent of concentration (Supplemental Table S2). Molecular weights calculated from S and D showed that M1-12 is a monomer and M1-13 is a discrete oligomer of six to eight subunits, depending on the value of D used in the calculation (Table 1 and Supplemental Table S2). Using the most reliable value of D, we find that the molecular weight of 403 kDa indicates that M1-13 is most likely an octamer. The frictional ratio (f/f_0) shows that M1-13 octamers are more symmetrical than M1-12 monomers (Table 1), suggesting that the octamers of M1-13 form by lateral association of elongated monomers. Octamers of M1-13 showed secondary structure by circular dichroism (CD) spectroscopy (Supplemental Figure S1C).

A larger Mid1p fragment consisting of domains 1–4 (M1-14) was soluble and showed secondary structure by CD spectroscopy (Figures 1D and Supplemental Figure S1D) but sedimented as multiple species (Supplemental Figure S2, C and D). M1-14 consists of only ~30% more amino acids than M1-13, but about half of M1-14 sedimented approximately five times faster than M1-13 (compare Supplemental Figure S2, B and C), and so these higher-order oligomers of M1-14 contain more than eight subunits (Supplemental Figure S2, C and D). On the other hand, construct M1-124 (M1-14 lacking domain M1-3) sedimented as two species, neither of which, based on estimated molecular weights, is an oligomer (Supplemental Figure S2E and Supplemental Table S2).

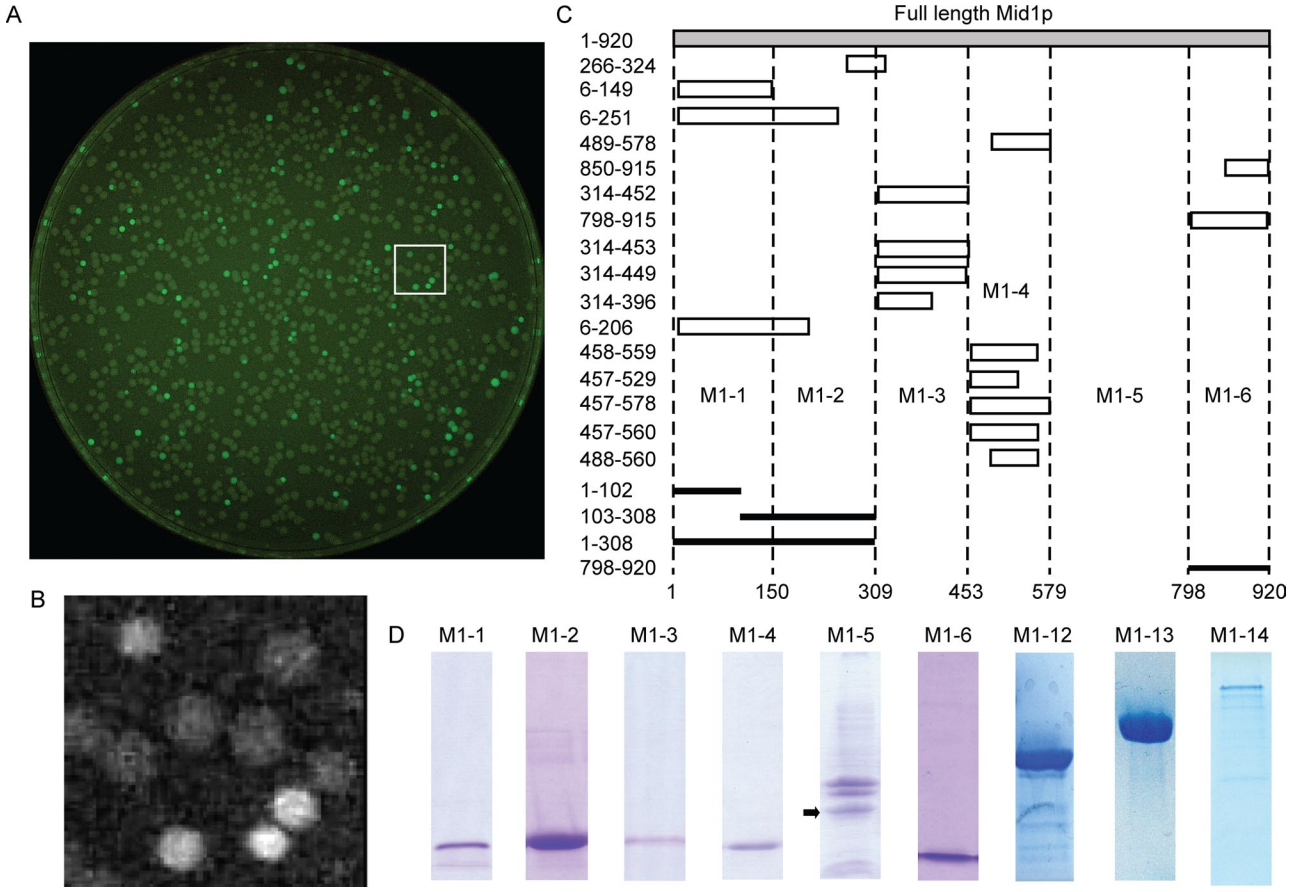

FIGURE 1: Five soluble domains and one insoluble domain account for entire length of Mid1p. (A) Fluorescence image of a Petri dish of *E. coli* colonies expressing a library of Mid1 cDNA fragments fused to mEGFP. Cells were transformed with constructs coding for fusion proteins consisting of random sections of Mid1 fused to the N-terminus of mEGFP, grown on LB agar plates containing 0.1 mg/ml ampicillin and 0.2 mM IPTG at 37°C for 18 h followed by 24 h at 33°C, and imaged under UV illumination. (B) Grayscale image of the box in A. (C) Map of 20 Mid1p fragments that produced fluorescent *E. coli* colonies when expressed fused upstream of mEGFP. The left column lists N- and C-terminal boundaries of each fragment. The open bars represent Mid1p fragments identified in the bacterial expression screen. The filled bars are domains predicted by the DomPred Protein Domain Prediction Server. Broken lines represent approximate domain boundaries. The boundary residue numbers are listed below the broken lines. (D) SDS–PAGE of Mid1p domains purified from *E. coli*. M1-1 (residues 1–149), M1-2 (150–308), M1-3 (309–452), M1-4 (453–578), M1-6 (798–920), M1-12 (1–308), M1-13 (1–452), and M1-14 (1–578) were soluble and purified by a combination of Ni-NTA affinity, ion-exchange, and size-exclusion chromatography, optimized for each construct. M1-5 (579–797) was insoluble in bacterial lysates made in 50 mM sodium phosphate, 300 mM NaCl, and 10 mM imidazole, pH 8.0 (black arrow). See also Supplemental Figure S1.

Complementation of cell division defects in Δ*mid1* cells with Mid1p deletion constructs

We used complementation experiments to assay the ability of six constructs lacking single domains of Mid1p to correct the abnormal position and orientation of the septum in Δ*mid1* cells (Figure 3). All six constructs mitigated these defects, but to different extents. The ability of these deletion constructs to correct the position of the septum correlated with their ability to correct the orientation of the septum (linear fit; $r^2 = 0.83$; Figure 3O), and the variability of both parameters among cells scaled inversely with the ability of each construct to correct both defects. The outcomes in cells depending on Mid1p lacking domain M1-2, M1-3, M1-4, or M1-6 were equal to those with full-length Mid1p, but cells divided more slowly than normal with Mid1p constructs lacking single domain M1-2, M1-4, or M1-6 (Supplemental Table S3). The construct lacking the N-terminal domain M1-1 (even with an added nuclear export sequence) was the least active, whereas the construct without insoluble domain M1-5 corrected most but not all of the defects. Thus M1-1 is the most important Mid1p domain for cytokinesis.

Localization of constructs composed of Mid1p domains

We used confocal microscopy of live Δ*mid1* cells to study the intracellular distributions of 16 different constructs consisting of one or more Mid1p domains fused to a fluorescent protein (Figure 4).

Localization to the nucleus. As expected from the presence of nuclear localization sequences in residues 450–506 (Almonacid *et al.*, 2009) and 691–695 (Paoletti and Chang, 2000), construct M1-4 concentrated inside the nucleus (Figure 4L) and insoluble domain M1-5 associated with the nuclear envelope (Figure 4M). M1-13 and three other single domains (M1-2, M1-3, and M1-6) targeted mEGFP, 2mEGFP, or tdTomato to the nucleus but to a lesser extent than did M1-4 (Figure 4, J–L, N, and P). However, the combination of domains M1-2, M1-3, M1-5, and M1-6 was

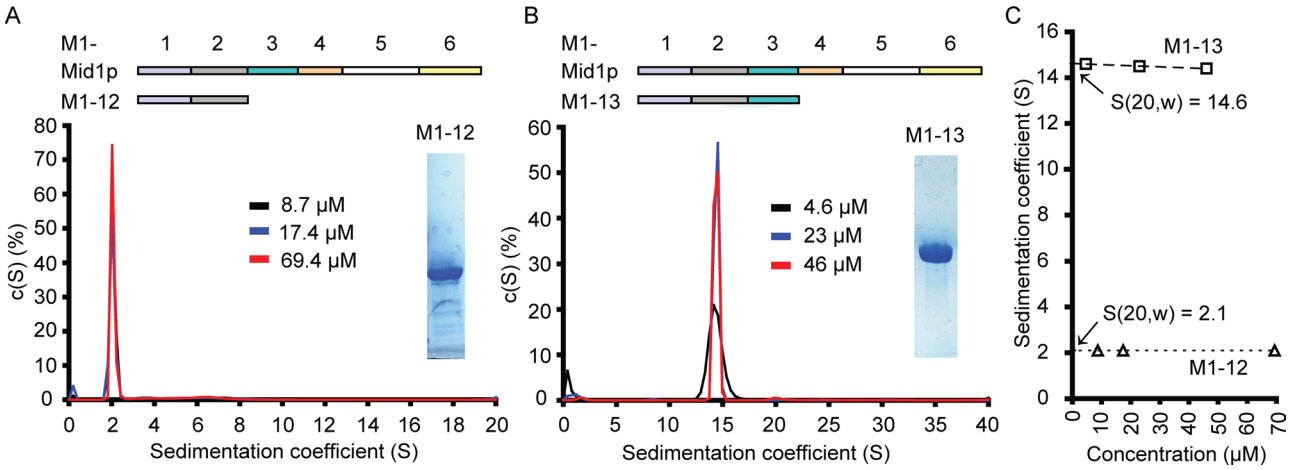

FIGURE 2: Analysis of Mid1p constructs by sedimentation velocity analytical ultracentrifugation. (A, B) Distributions of sedimentation coefficients, assuming a continuous *c*(*S*) distribution. Bin width: 1/100 of the range of sedimentation coefficients plotted. Insets show cartoons defining M1-12 and M1-13 and SDS–PAGE of recombinant M1-12 and M1-13 stained with Coomassie blue. (A) Three concentrations of M1-12 (residues 1–308): black, 8.7 μM; blue, 17.4 μM; and red; 69.4 μM. Conditions: 42,000 rpm in 20 mM Tris, 150 mM NaCl, 1 mM TCEP, pH 8.0, at 20°C. (B) Three concentrations of M1-13 (residues 1–452): black, 4.6 μM; blue, 23.0 μM; and red, 46.0 μM. Conditions: 28,000 rpm in 20 mM Tris, 150 mM NaCl, and 1 mM TCEP, pH 7.3, at 20°C. (C) Dependence of sedimentation coefficients on the concentrations of (triangles) M1-12 and (squares) M1-13. The *y*-intercepts of linear fits represent sedimentation coefficients at 20°C in water ($S_{20,w}$). See also Supplemental Figure S2.

insufficient to concentrate M1-Δ4 or a Mid1p nuclear shuttling mutant (Almonacid *et al.*, 2009) in the nucleus (Figure 4F), so any nuclear localization sequences in these domains must be weak in the context of the full-length protein.

Localization to nodes. In late interphase and mitosis, the nuclear export sequence (NES) in M1-1 (residues 69–81; Paoletti and Chang, 2000) allows Mid1p to leave the nucleus and localize to nodes in the cortex. We define nodes to be punctate structures in the cortex that condense into a contractile ring or structures that eventually form a contractile ring. No single Mid1p domain could localize 2mEGFP or tdTomato to nodes (Figure 4, I–N), so some combination of the six domains mediates localization in nodes. We used deletion constructs to identify these domains. Mid1p constructs lacking domain M1-2, M1-3, M1-4, M1-5, or M1-6 localized to nodes (Figure 4, D–H). The Mid1p construct lacking the N-terminal domain M1-1 (with an added nuclear export sequence) localized to punctate structures in the cortex generally surrounding the nucleus, but in contrast to nodes, these puncta did not condense into a contractile ring (Figure 4C), similar to Mid1p constructs with mutations or deletions in domain M1-1 (Almonacid *et al.*, 2011). Therefore domain M1-1 is required but not sufficient to localize full-length Mid1p to nodes. M1-13 consisting of domains M1-1 through M1-3 was the smallest Mid1p construct that concentrated in nodes (Figure 4P). The construct Mid1p (300–450) consisting of nine residues of M1-2 and most of M1-3 localized to punctate structures in the medial cortex (Almonacid *et al.*, 2009), but it was unclear whether these puncta contributed to assembly of the contractile ring.

Restriction of cortical Mid1p to nodes. Insoluble domain M1-5 on its own spread throughout the cortex (Figure 4M), but it did not concentrate in nodes around the equator. This behavior suggests that other Mid1p domains help restrict full-length Mid1p to nodes. The presence of domain M1-1 allowed the constructs lacking domain M1-2, M1-3, M1-4, M1-5, or M1-6 to concentrate in nodes (Figure 4, D–H), but the constructs lacking domain M1-3 or M1-4 also spread diffusely throughout the cortex (Figure 4, E and F). Therefore the presence of domains M1-3 and M1-4 in addition to M1-1 ensures that full-length Mid1p concentrates in the cortex exclusively in nodes.

Mid1p construct	Stokes radius (Å) from gel filtration	*D* from R_s ($cm^2\ s^{-1}$)	*D* from centrifugation ($cm^2\ s^{-1}$)	$S_{20,w}$ from centrifugation	Molecular weight (kDa)	Order of oligomerization	f/f_0
1–308 (M1-12)	45.7 ± 2.2	4.70×10^{-7}	4.97×10^{-7}	2.1	36.8	1.0	2.0
1–452 (M1-13)	62.5 ± 1.5	3.43×10^{-7}	3.18×10^{-7}	14.6	403.2	7.9	1.4

Conditions are given in the legend of Figure 2. The following notation is used in the equations given here: Stokes radius (R_s), diffusion coefficient (*D*), sedimentation coefficient at 20°C in water ($S_{20,w}$), Boltzmann constant (k_B), temperature in degrees kelvin (*T*), buffer viscosity (η), Avogadro's number (N_A), partial specific volume of Mid1p constructs (ν), buffer density (ρ), and molecular weight (*M*). The SEDNTERP software was used to estimate the values of ρ and η from buffer composition, and ν from amino acid composition. The Stokes radius was measured on calibrated size-exclusion columns, and the values given are averages ± SD from four independent measurements. *D* was estimated in two ways: from R_s using the relationship $D = k_B T/(6\pi\eta R_s)$ and from diffusive boundary spreading during sedimentation velocity ultracentrifugation (see Supplemental Table S2). The signal-to-noise ratio in centrifugation was better at high concentrations, so this table lists values of *D* for 69.4 μM M1-12 and 46.0 μM M1-13. The $S_{20,w}$ values are the *y*-intercepts of linear fits of sedimentation coefficients vs. concentration (Figure 2C). *M* was calculated from $S_{20,w}$ and *D* (from centrifugation): $M = S_{20,w}/D.\ N_A k_B T/(1 - \nu\rho)$. Orders of oligomerization were calculated from molecular weights divided by subunit molecular weights calculated from amino acid compositions. Frictional ratio $f/f_0 = S_{sphere}/S_{20,w}$, where $S_{sphere} = M(1 - \nu\rho)/\{6\pi\eta N_A[3M\nu/(4\pi N_A)]^{1/3}\}$(Lebowitz *et al.*, 2002).

TABLE 1: Hydrodynamic properties of Mid1p constructs.

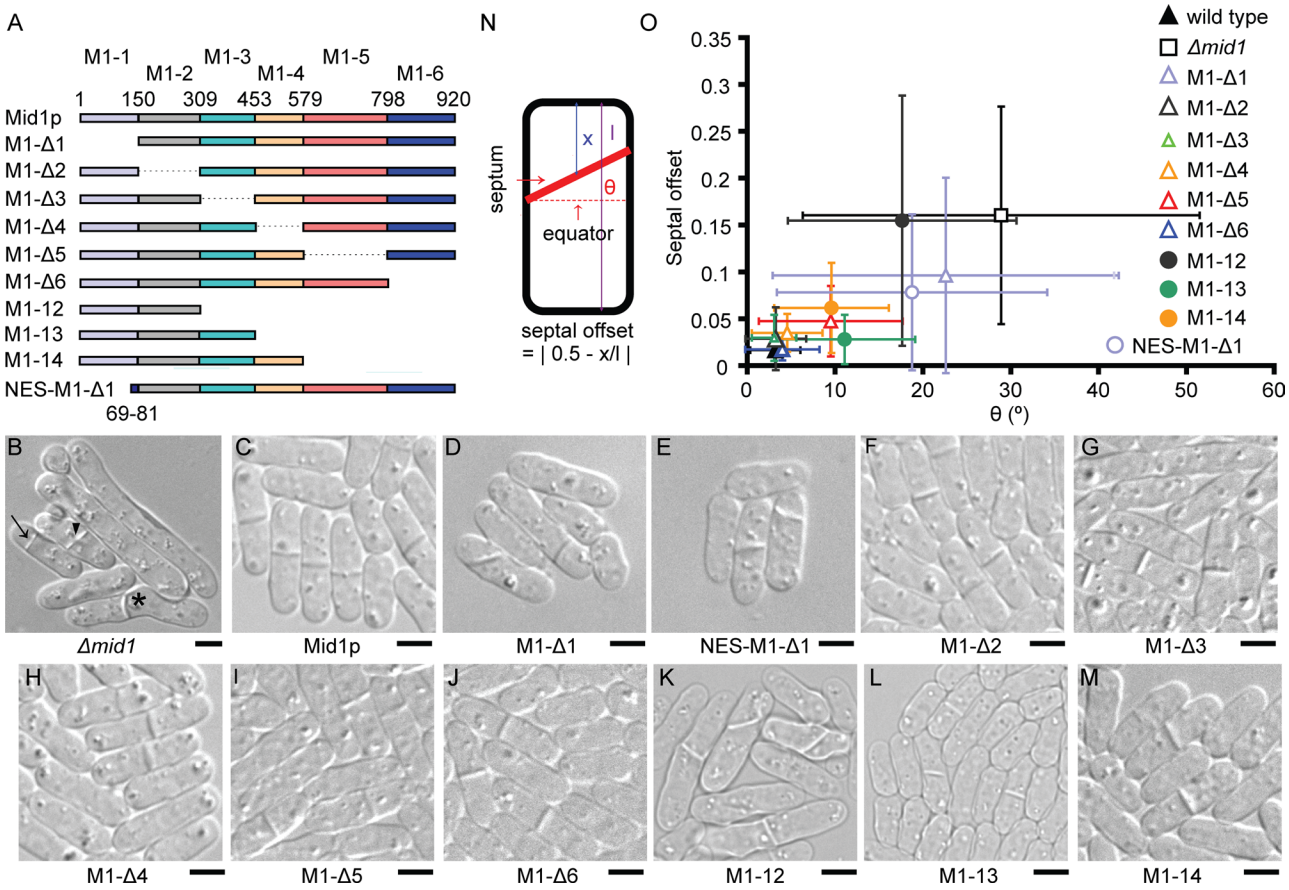

FIGURE 3: Complementation of defects in septal geometry in Δ*mid1* cells by expression of Mid1p-deletion constructs. (A) Map of Mid1p constructs. Broken lines represent domain deletions. NES-M1-Δ1 includes a nuclear exit sequence (Mid1p residues 69–81) upstream of M1-Δ1. (B–M) Differential interference contrast (DIC) micrographs. (B) Δ*mid1* cells with misplaced (arrow), misoriented (arrowhead), and curved (star) septa. (C) Cells expressing Mid1p-mEGFP from the *mid1* locus. (D–M) Δ*mid1* cells expressing (D) M1-Δ1-2mEGFP from the *mid1* locus, (E) NES-M1-Δ1-2mEGFP from the *mid1* locus, (F) M1-Δ2-2mEGFP from the *mid1* locus, (G) M1-Δ3-mEGFP from a *mid1* promoter in the *leu1* locus, (H) M1-Δ4-mEGFP from a *mid1* promoter in the *leu1* locus, (I) M1-Δ5-mEGFP from a *mid1* promoter in the *leu1* locus, (J) M1-Δ6-2mEGFP from the *mid1* locus, (K) M1-12-tdTomato from the *mid1* locus, (L) M1-13-mEGFP from a *mid1* promoter in the *leu1* locus, and (M) M1-14-tdTomato from the *mid1* locus. (N) Cartoon of *S. pombe* defining septal offset and septum tilt angle θ. (O) Comparison of septal offset and tilt angles in complementation experiments. Cylindrical or near-cylindrical cells containing a single septum were scored. The larger value of θ was scored for curved septa intersecting two sides of a cell at different angles. Error bars are 1 SD. (▲, $n = 33$) Wild-type cells. (□, $n = 47$) Δ*mid1* cells. Δ*mid1* cells expressing from the *mid1* locus, (△, $n = 62$) M1-Δ1-2mEGFP, (△, $n = 26$) M1-Δ2-2mEGFP, (△, $n = 33$) M1-Δ6-2mEGFP, (δ, $n = 37$) M1-12-tdTomato, (δ, $n = 33$) M1-14-tdTomato, or (σ, $n = 35$) NES-M1-Δ1-2mEGFP. Δ*mid1* cells expressing from a *mid1* promoter in the *leu1* locus (△, $n = 35$) M1-Δ3-mEGFP, (△, $n = 19$) M1-Δ4-mEGFP, (△, $n = 39$) M1-Δ5-mEGFP, or (δ, $n = 51$) M1-13-mEGFP. The cartoon in N and the values of septal offset and tilt angle in wild-type and Δ*mid1* cells are reproduced from Saha and Pollard (2012). Scale bars, 5 μm.

Localization to contractile rings. Most but not all Mid1p constructs that localized to nodes also concentrated in contractile rings, whereas no Mid1p construct missing from nodes concentrated in contractile rings. Both constructs M1-Δ6 (Mid1p lacking domain M1-6) and M1-14 (Mid1p lacking domains M1-5 and M1-6) localized to nodes, and nodes marked with M1-Δ6 condensed into contractile rings, but we did not detect M1-14 in contractile rings (Figures 4H and 5A). Therefore insoluble domain M1-5 may be required in addition to domain M1-1 (required for localization to nodes) for Mid1p to localize to contractile rings.

Localization near septa. Mid1p normally disappears from the contractile ring before the onset of constriction (Wu *et al.*, 2003), but we found that small amounts of Mid1p and constructs NES-M1-Δ1, M1-Δ2, M1-Δ3, M1-Δ4, M1-Δ5, M1-Δ6, M1-13, and M1-14 localized near septa in some cells (Figures 4P and 5A and Supplemental Figure S3). These structures marked with M1-13 or M1-Δ5 appeared to constrict over time (Supplemental Figure S3, H and I). Reconstructions of cells showed that M1-13 concentrated in a disk rather than in the contractile ring marked with Rlc1p-mCherry (Supplemental Figure S3I).

Contractile ring assembly in cells depending on Mid1p constructs lacking domain M1-5

In cells depending on Mid1p constructs lacking the insoluble domain M1-5, the pathway of contractile ring assembly from nodes was abnormal. Surprisingly, three of our Mid1p constructs that lack domain M1-5 (M1-13, M1-14, and M1-Δ5) restored the normal

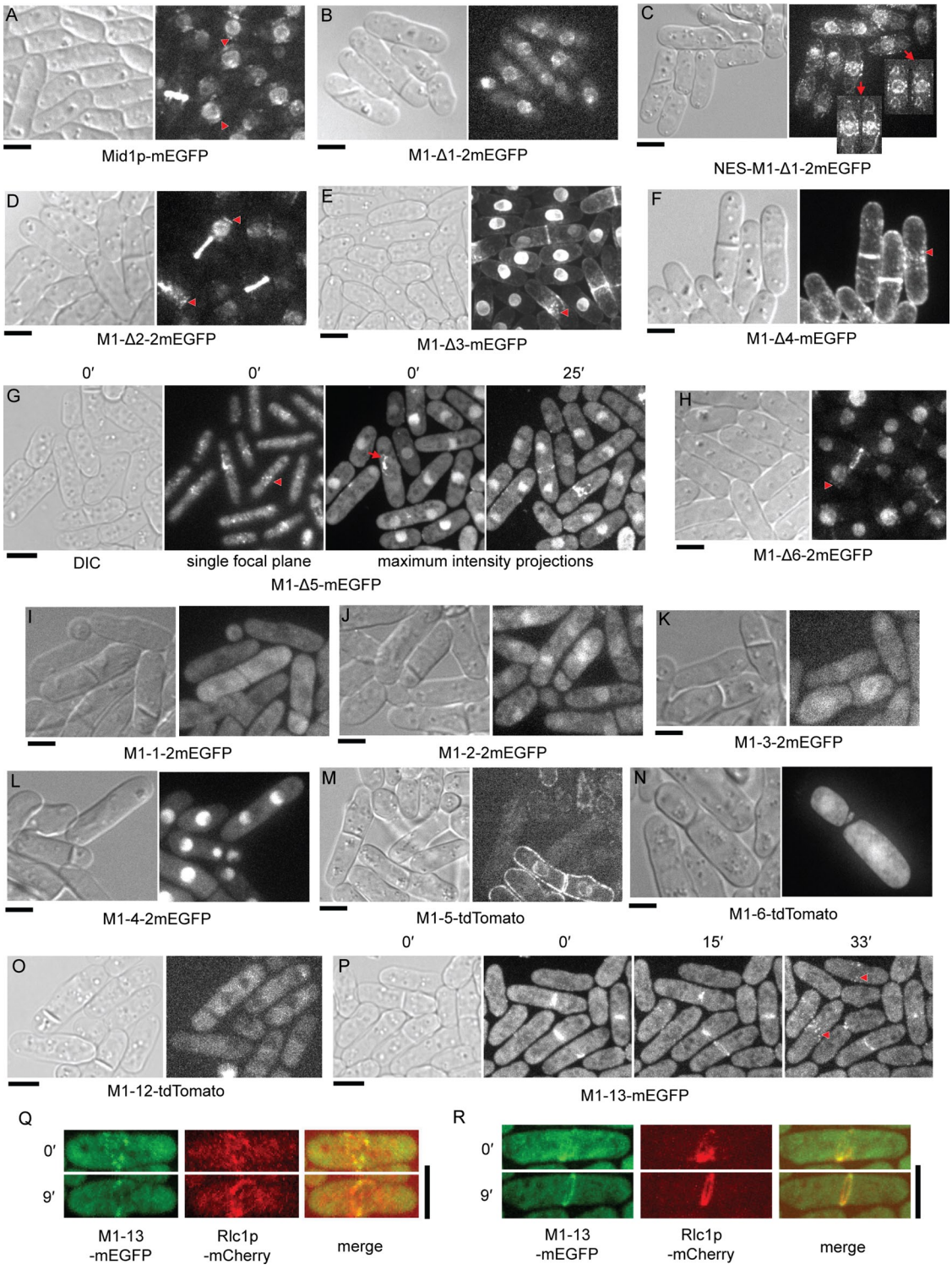

FIGURE 4: Intracellular localization of Mid1p constructs. Red arrowheads show nodes in the cortex. (A–F, H–J, L, N, O) Pairs of DIC and maximum-intensity projection fluorescence micrographs of cells expressing Mid1p or various Mid1p deletion constructs tagged with fluorescent proteins. (A) Cells expressing Mid1p-mEGFP from the *mid1* locus. (B–F) Δ*mid1* cells expressing (B) M1-Δ1-2mEGFP from the *mid1* locus, (C) NES-M1-Δ1-2mEGFP from the *mid1* locus (inset shows medial focal planes of two cells indicated by arrows), (D) M1-Δ2-2mEGFP from the *mid1* locus, (E) M1-Δ3-mEGFP from a *mid1* promoter in the *leu1* locus, and (F) M1-Δ4-mEGFP from a *mid1* promoter in the *leu1* locus. (G) Micrographs of Δ*mid1* cells expressing M1-Δ5-mEGFP from a *mid1* promoter in the *leu1* locus at two time points: the three panels at time 0 show (left) a DIC micrograph, (middle) fluorescence micrograph of a single focal plane close to the cortex, and (right) a maximum-intensity projection fluorescence micrograph of a stack of confocal sections, and at time 25 min a maximum-intensity projection fluorescence micrograph. M1-Δ5-mEGFP concentrates in nodes (arrowhead) and strands (arrow). (H–J) Δ*mid1* cells expressing (H) M1-Δ6-2mEGFP from the *mid1* locus, (I) M1-1-2mEGFP from the *mid1* locus,

position of septa close to the equator in Δ*mid1* cells in spite of a defective pathway of ring assembly (Figure 3, I, L, M, and O).

Formation of nodes. Constructs M1-13 and M1-14 localized to nodes containing Myo2 around the equator in mitotic cells (Figures 4, P and Q, and 5, A and J). In cells depending on M1-14, nodes with Blt1p localized normally, close to the new pole immediately after cell division and then dispersed in the cortex before concentrating around the equator (Figure 5B). M1-14 shuttled out of the nucleus and joined Blt1p in equatorial nodes that accumulated Myo2 and formin Cdc12p (Figures 5, A, B, D, F, and I–K, and 6, B–D), although Myo2 arrived ~10 min late (Figure 5L). These cytokinetic nodes were positioned more normally than in Δ*mid1* cells with mean positions (±SD) of 0.05 ± 0.16 for Blt1p nodes, 0.03 ± 0.13 for Rlc1p nodes, and 0.02 ± 0.06 for Cdc12p nodes (Figure 6, B–D).

Assembly of contractile ring from nodes. Despite near-normal starting conditions with nodes around the equator and good final outcomes with centrally placed septa, cells depending on M1-13 or M1-14 did not assemble contractile rings normally, accounting for the more variable orientation of the septa than normal (Figure 3O). In cells depending on M1-13, nodes containing Myo2 initially coalesced into strands that eventually formed the contractile ring (Figure 4, Q and R). We studied ring assembly in more detail in the M1-14 strain than the M1-13 strain. Starting from apparently normal initial conditions (equatorial nodes containing both Myo2 and Cdc12p), the nodes formed one or more strands containing M1-14, Blt1p, Myo2, and Cdc12p (Figure 5, A, C, D, F, and G). These strands slowly closed into a ring in most cells over the same median time of 32 min as strands in Δ*mid1* cells (Figure 5, D–F and L). The outcome in terms of the position and orientation of the rings (Figure 3O) was much better than in Δ*mid1* cells because the strands were generally confined within a narrow zone around the equator (Figure 5E and Supplemental Video S1), in contrast to being dispersed over a larger area of the cortex in Δ*mid1* cells (see accompanying article, Saha and Pollard, 2012). M1-14 was not detected in complete contractile rings. Similar to Δ*mid1* cells, rings in M1-14 cells constricted as soon as strands closed into rings (Figure 5, E, H, and L).

Insoluble domain M1-5 is the more important of the two Mid1p domains missing in M1-14 because the outcomes were indistinguishable in cells depending on M1-14 or M1-Δ5 (Figure 3O), whereas cells depending on M1-Δ6 had outcomes similar to cells depending on full-length Mid1p (Figure 3O). Nodes in cells dependent on Mid1p without domain M1-5 initially formed strands rather than directly condensing into a contractile ring (Figure 4G). We did not detect Mid1p constructs lacking domain M1-5 in contractile rings that formed slowly from strands, perhaps because these constructs no longer associated with contractile rings ~30 min after spindle pole body separation like full-length Mid1p (Wu *et al.*, 2003).

Contributions of Mid1p domains to cellular morphology and polarity

We tested the ability of various Mid1p constructs to correct the defects in cellular morphology and polarity in Δ*mid1* cells reported in the accompanying article (Saha and Pollard, 2012). These defects include branches, curves, and ectopic bulges, along with some loss of polarization of Tea1p-mEGFP (compare Figure 7, A and B).

Complementation experiments showed that 9 of 10 Mid1p constructs with domain deletions corrected most morphological defects of many Δ*mid1* cells (Figure 7E). The ability of these constructs to correct septal placement defects was correlated directly with their ability to correct defects in cellular morphology (linear fit; $r^2 = 0.88$; Figure 7E). The tiny construct M1-12 had limited capacity to correct the morphological defects, whereas M1-13 and M1-Δ1 had substantial effects on morphology (Figure 7E). Although M1-12 and M1-Δ1 are equally limited in their ability to correct septal defects in Δ*mid1* cells, M1-Δ1 corrected the morphological defects better than M1-12. This difference suggests that defects in cytokinesis may not be the only cause of morphological defects in Δ*mid1* cells.

Both M1-Δ1 and M1-14 mitigated the defects with polarization of Tea1p in Δ*mid1* cells. In cells depending on these Mid1p constructs the localization of Tea1p-mEGFP at the poles was more focused than in Δ*mid1* cells, but a few discrete Tea1p dots also scattered away from the poles (Figure 7, C and D). Thus some combination of domains M1-2, M1-3, and M1-4 helps to maintain polarity.

DISCUSSION

Identification of five soluble domains and one insoluble domain of the large Mid1p protein opened up biophysical studies and improved the design and simplified the interpretation of biological experiments, but crystal structures will be required to establish the domain architecture definitively. Figure 8 summarizes the roles of Mid1p domains in cytokinesis, and Figure 9 compares our complementation experiments with previous studies that used constructs composed of arbitrary pieces of Mid1p. In spite of the arbitrary design, many of these pieces sufficed for some aspects of the intracellular localization or functions of full-length Mid1p because they were large and contained many of the Mid1p domains that mediate an impressively redundant network of interactions. Our work helps to map these interactions to individual domains and to verify direct interactions between Cdr2p (Almonacid *et al.*, 2009), Gef2p (Ye *et al.*, 2012), or Clp1p (Clifford *et al.*, 2008) and specific parts of Mid1p (Figure 9) as suggested mainly based on loss-of-interaction deletions in Mid1p.

We show for the first time that the Mid1p construct M1-13 (residues 1–452) forms homogeneous octamers that carry out many of the functions of the full-length protein. Oligomerization may contribute to the activity of Mid1p as a scaffold for other proteins in cytokinetic nodes and contractile rings. M1-13 lacks the insoluble

and (J) M1-2-2mEGFP from the *mid1* locus. (K) DIC and a medial confocal section fluorescence micrograph of Δ*mid1* cells expressing M1-3-2mEGFP from the *mid1* locus. (L) Δ*mid1* cells expressing M1-4-2mEGFP from the *mid1* locus. (M) DIC and medial focal plane fluorescence micrograph of Δ*mid1* cells expressing M1-5-tdTomato for 16 h from a *3xnmt1* promoter in the *leu1* locus. (N) Δ*mid1* cells expressing M1-6-tdTomato for 18 h from a *3xnmt1* promoter in the *leu1* locus. (O) Δ*mid1* cells expressing M1-12-tdTomato from the *mid1* locus. (P–R) Δ*mid1* cells expressing M1-13-mEGFP from a *mid1* promoter in the *leu1* locus and Rlc1p-mCherry from the *rlc1* locus. (P) DIC and time-lapse maximum-intensity projection fluorescence micrographs (green channel only). (Q, R) Time-lapse two-dimensional projections of fluorescence micrographs. (Q) Nodes containing M1-13-mEGFP and Rlc1p-mCherry form strands. Planes of image projection at 0 and 9 min are rotated 240° with respect to each other around the long axis of the cell. (R) Strands containing Rlc1p-mCherry form contractile ring. Scale bars, 5 μm. See also Supplemental Figure S3.

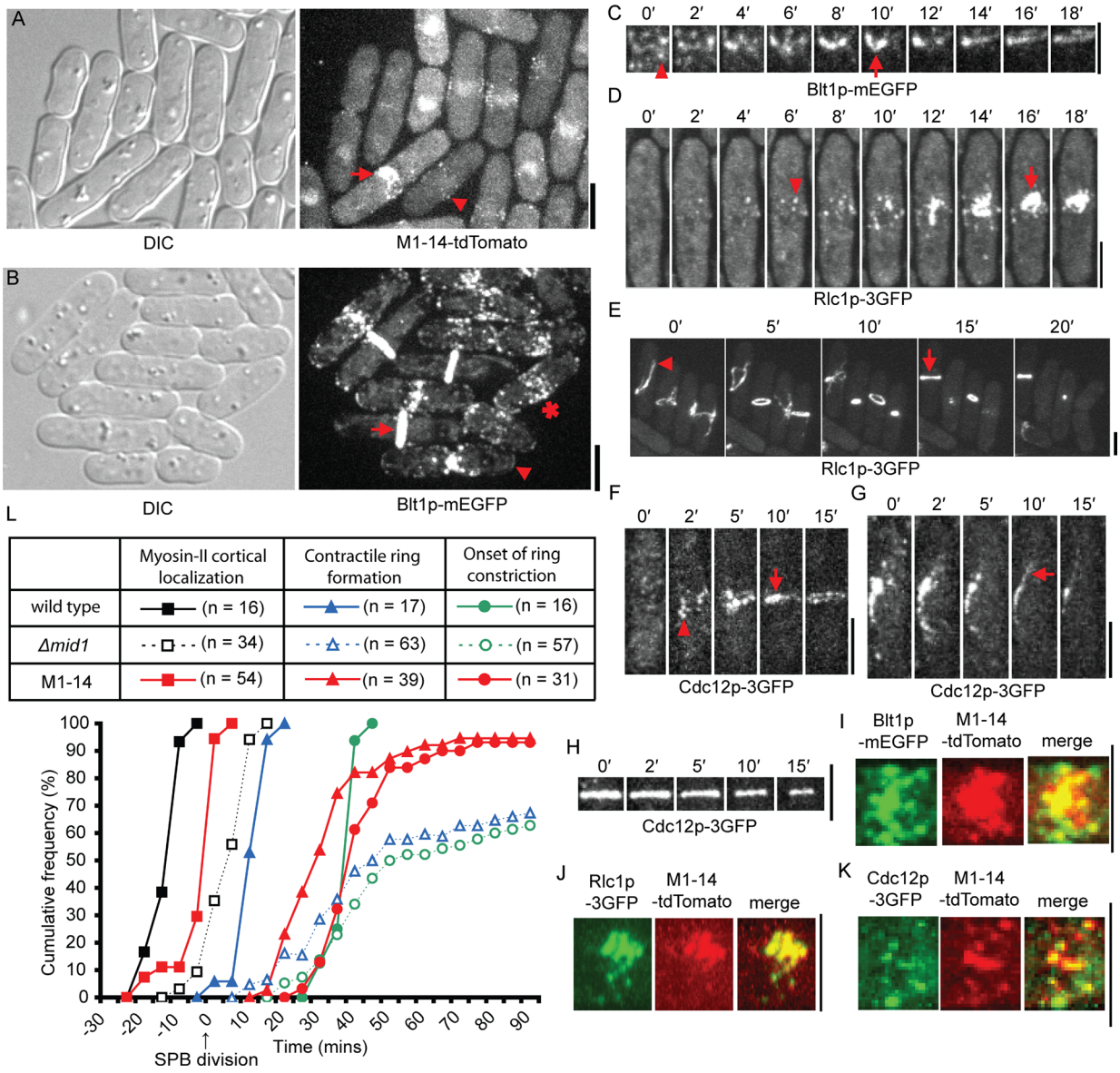

	Myosin-II cortical localization	Contractile ring formation	Onset of ring constriction
wild type	■ (n = 16)	▲ (n = 17)	● (n = 16)
Δmid1	□ (n = 34)	△ (n = 63)	○ (n = 57)
M1-14	■ (n = 54)	▲ (n = 39)	● (n = 31)

FIGURE 5: Assembly of contractile rings in Δ*mid1* cells expressing Mid1p (1–578; M1-14). (A–K) Δ*mid1* cells expressing M1-14-tdTomato from the *mid1* locus. (A, B) Pairs of DIC and maximum-intensity projection fluorescence micrographs showing the localization of (A) M1-14-tdTomato and (B) Blt1p-mEGFP. M1-14-tdTomato localizes to nodes in the cortex surrounding the nucleus (A, arrowhead) and strands (A, arrow). Nodes of Blt1p concentrate near the new pole of short cells (B, arrowhead), form a broad band at the cell equator in long cells (B, star), and eventually form contractile rings (B, arrow). (C) Time-lapse maximum-intensity projection fluorescence micrographs of the equatorial region of a cell showing nodes with Blt1p (arrowhead) coalesce into strands (arrow) that eventually close into a ring. The long axis of the cell is vertical. (D, E) Time-lapse two-dimensional projections of fluorescence micrographs showing the generation of (D) strands (arrow) from nodes (arrowhead) and (E) contractile ring (arrow) from strands (arrowhead) marked by Rlc1p-3GFP. Images in D show a single cell with the long axis vertical, and E show many cells. (F–H) Time-lapse maximum-intensity projection fluorescence micrographs show (F) nodes (arrowhead) coalescing into strands (arrow) that eventually close into a ring, (G) an elongated strand (arrow), and (H) constriction of a contractile ring marked by Cdc12p-3GFP. Images in F and G show single cells with their long axes vertical, and H shows the equatorial region of a cell containing the ring. (I–K) Fluorescence micrographs of the equator showing colocalization of M1-14-tdTomato and (I) Blt1p-mEGFP, (J) Rlc1p-3GFP, and (K) Cdc12p-3GFP. Images in I and K are maximum-intensity projections; J is a two-dimensional projection in a plane tilted 30° from the *xy*-plane. (L) Time courses of recruitment of myosin-II to the cortex and formation and constriction of the contractile ring relative to the time of spindle pole body division tracked by Sad1p-mRFP1 or Sad1p-mEGFP defined as time zero. Appearance of Rlc1p-mEGFP in the cortex in (□, $n = 34$) Δ*mid1* or Rlc1p-3GFP in (■, $n = 16$) wild-type and (■, $n = 54$) M1-14 cells; formation of contractile ring (tracked by Rlc1p-mEGFP or Rlc1p-3GFP) in (▲, n = 17) wild-type, (△, n = 63) Δ*mid1*, and (▲, n = 39) M1-14 cells; onset of contractile ring constriction (tracked by Rlc1p-mEGFP or Rlc1p-3GFP) in (●, n = 16) wild-type, (○, n = 57) Δ*mid1*, and (●, n = 31) M1-14 cells. Bin width, 5 min. The sample included only cells for which Rlc1p persisted in the cortex long enough to document formation of strands or rings. Data on timing of cytokinetic events in wild-type and Δ*mid1* cells are reproduced from Saha and Pollard (2012). Scale bars, 5 μm. See also Supplemental Video S1.

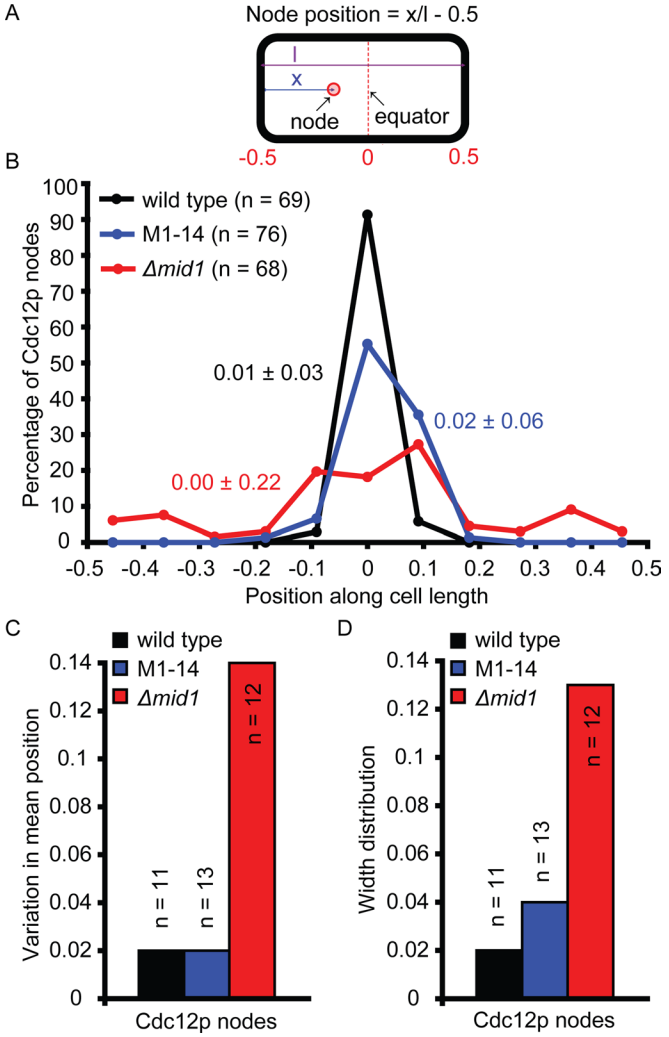

FIGURE 6: Positions of cytokinetic nodes in wild-type, Δ*mid1*, and Δ*mid1* cells expressing Mid1p (1–578; M1-14). (A) Cartoon of *S. pombe* defining node position. (B) Histogram showing distributions of nodes marked with Cdc12p-3GFP in mitosis, scored in maximum-intensity projection fluorescence micrographs. Data from multiple cells were pooled together and distributed into bins of width 1/11 of the cell length. The frequency was normalized to the total number of nodes and plotted at the midpoint of each bin. Mean ± SD node positions are color coded to match that of the distribution of different types of nodes. •, Wild-type cells ($n = 69$ from 11 cells); •, M1-14 cells ($n = 76$ from 13 cells); and •, Δ*mid1* cells ($n = 68$ from 12 cells). (C, D) Comparison of the distribution of Cdc12p node positions among (■) 11 wild-type, (■) 13 M1-14, and (■) 12 Δ*mid1* cells from data shown in B. (C) Histogram showing the variation in center of the distribution. In each cell, the mean position of nodes containing Cdc12p was calculated. The SD among cells in these mean positions is plotted. (D) Histogram showing the width of the distribution expressed as the average among cells in the SD of position of nodes containing Cdc12p. In each cell, the SD among positions of nodes containing Cdc12p was calculated. The mean of these SD values across cells is plotted. The cartoon in A and the data on the position of Cdc12p nodes in wild-type and Δ*mid1* cells in B–D are reproduced from Saha and Pollard (2012).

domain M1-5 that is required for the normal, efficient condensation of nodes directly into the contractile ring. It is surprising that in spite of the defects in the pathway of ring assembly in absence of M1-5, restriction of contractile ring precursors in nodes within a narrow zone around the equator of cells depending on M1-14 (residues 1–578) suffices to reliably place the plane of cell division close to the equator.

Contributions of Mid1p domains to oligomerization

Domain M1-3 (residues 309–452) allows the Mid1p fragment M1-13 (residues 1–452) to form homogeneous, relatively compact octamers. M1-3 most likely supports oligomerization of full-length Mid1p in fission yeast cells because the concentration of Mid1p in mature contractile rings is >4 μM (Wu and Pollard, 2005), well above the concentration where M1-13 octamers are stable (Figure 2B). Further support comes from quantitative fluorescence measurements in live cells, where nodes transition early in mitosis from having ~17 to ~28 molecules of full-length Mid1p tagged with monomeric yellow fluorescent protein (Laporte *et al.*, 2011). This quantal change can be explained by interphase nodes with two octamers of Mid1p acquiring one or two additional octamers of Mid1p during mitosis.

The behavior of Mid1p oligomers in detergent extracts of whole cells (Celton-Morizur *et al.*, 2004) is consistent with the behavior of purified M1-13 with a sedimentation coefficient of 14.6 S. In extracts, construct Mid1p (1–506), similar to M1-13 but with an additional 54 residues of M1-4, sedimented at ~12 S (our calculation), similar to a small fraction of full-length Mid1p tagged to GFP (Celton-Morizur *et al.*, 2004). Full-length Mid1p and Mid1p (507–920, consisting of part of M1-4 through the C-terminus) were heterogeneous, with sedimentation coefficients ranging from 20 S to much higher values (our calculation). These constructs also self-associated in coimmunoprecipitation experiments (Celton-Morizur *et al.*, 2004).

Contributions of Mid1p domains to cytokinesis

Mid1p association with nodes. Individually none of the six domains of Mid1p targets 2mEGFP or tdTomato to nodes, and constructs lacking single domains except for M1-1 concentrate in nodes, so cooperation between M1-1 and different subsets of domains M1-2 through M1-6 suffice for interaction with nodes. Construct M1-13 is the smallest fragment of Mid1p that not only concentrates in nodes, but also supports reliable cytokinesis. Domain M1-3 cooperates with M1-1 to target M1-13 to nodes. Domain M1-2 does not suffice without domain M1-3, since construct M1-12 is absent from nodes. M1-3 may contribute to node association through direct interactions with partners or reactions dependent on oligomerization mediated by M1-3. A construct similar to M1-3 concentrated in punctate structures in the medial cortex (Almonacid *et al.*, 2009), but it is unclear whether these puncta contribute to assembly of the contractile ring. Constructs M1-Δ3 and M1-Δ4, lacking domains M1-3 or M1-4, localize to nodes, but a fraction of these proteins spread throughout the cortex, suggesting that interactions mediated by both these domains are required for full-length Mid1p to localize in the cortex exclusively in nodes.

Roles of interphase node proteins in recruiting Mid1p to nodes. M1-13 is soluble and does not bind diffusely to the cortex, so domains M1-1 through M1-3 likely interact with node proteins. The binding partners in interphase nodes for domains M1-1 and M1-2, if any, remain unknown. One candidate receptor in nodes for M1-3 is Cdr2p, which is proposed to recruit precursors to interphase nodes following a simple linear hierarchy: Cdr2p → (Blt1p, Mid1p) → contractile ring proteins (Martin and Berthelot-Grosjean, 2009; Moseley *et al.*, 2009). M1-3 may interact with Cdr2p or the putative Rho-GEF Gef2p because deletions in domain M1-3 weaken the

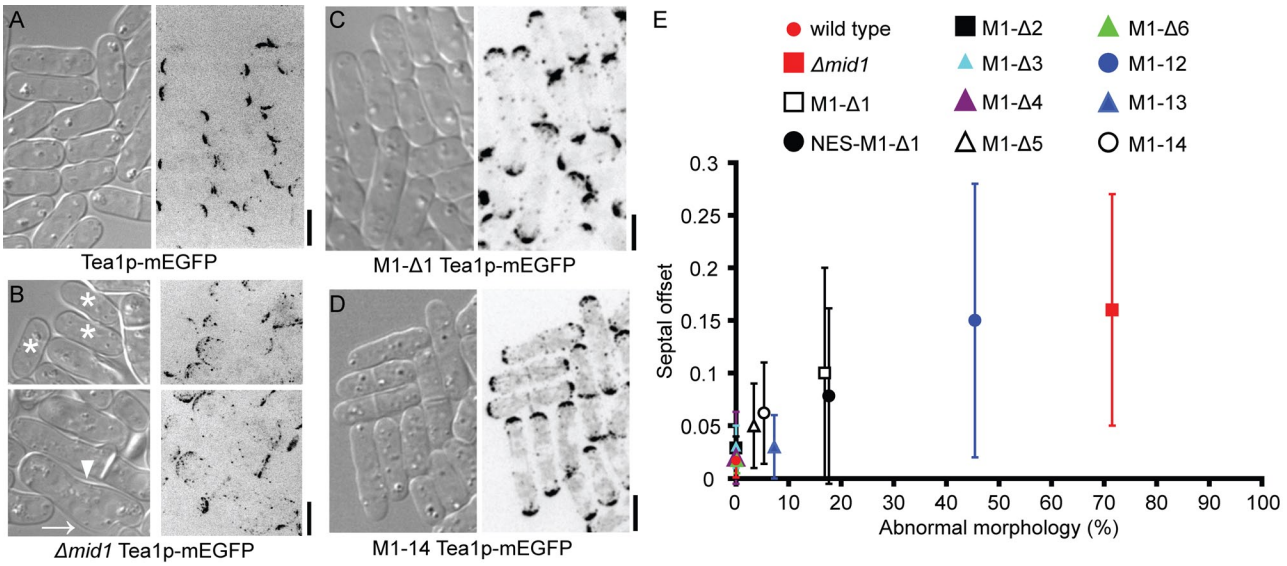

FIGURE 7: Complementation of defects in cell morphology and polarity of Δ*mid1* cells by expression of Mid1p-deletion constructs. (A–D) DIC and negative-contrast, maximum-intensity projection fluorescence micrographs of cells expressing Tea1p-mEGFP. (A) Wild-type cells, (B) Δ*mid1* cells with curves (arrowhead), branches, ectopic bulges (arrow), and more disperse localization of Tea1p at the poles of cylindrical cells (stars), (C) Δ*mid1* cells expressing M1-Δ1-tdTomato from the *mid1* locus, and (D) Δ*mid1* cells expressing M1-14-tdTomato from the *mid1* locus. (E) Plot of septal offset vs. percentage of cells with abnormal morphology. •, Number of cells scored for morphology (n_x) = 903 and number of septa scored (n_y) = 33 for wild-type cells; (■, n_x = 439 and n_y = 47) for Δ*mid1* cells and Δ*mid1* cells expressing from the *mid1* locus (□, n_x = 664 and n_y = 62) M1-Δ1-2mEGFP, (●, n_x = 283 and n_y = 35) NES-M1-Δ1-2mEGFP, (■, n_x = 605 and n_y = 26) M1-Δ2-2mEGFP, (▲, n_x = 627 and n_y = 33) M1-Δ6-2mEGFP, (○, n_x = 244 and n_y = 33) M1-14-tdTomato, or (●, n_x = 361 and n_y = 37) M1-12-tdTomato. Δ*mid1* cells expressing from a *mid1* promoter in the *leu1* locus (▲, n_x = 309 and n_y = 35) M1-Δ3-mEGFP, (▲, n_x = 233 and n_y = 19) M1-Δ4-mEGFP, (△, n_x = 665 and n_y = 39) M1-Δ5-mEGFP, or (▲, n_x = 672 and n_y = 51) M1-13-mEGFP. Error bars, 1 SD. Scale bars, 5 μm.

interaction of Mid1p with Cdr2p (Almonacid *et al.*, 2009) and Gef2p (Ye *et al.*, 2012) in coimmunoprecipitation experiments (Figure 9). Nevertheless, other interactions must contribute to the association of Mid1p with nodes because the construct M1-Δ3 lacking domain M1-3 localizes to nodes, and septa are placed correctly in cells depending on M1-Δ3 or in cells lacking Cdr2p (Almonacid *et al.*, 2009) or Gef2p (Ye *et al.*, 2012).

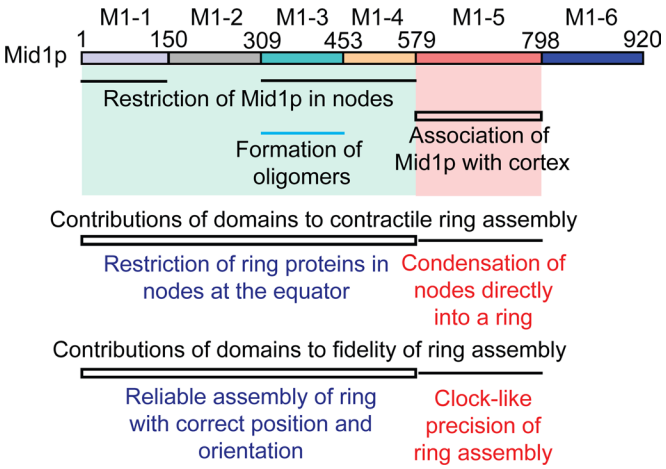

FIGURE 8: Role of Mid1p domains in cytokinesis. Black lines indicate domains of Mid1p required for the role denoted below each line. The blue line indicates that domain M1-3 is required to form oligomers of Mid1p constructs consisting of subsets of the first four domains of Mid1p (M1-1 through M1-4). Open rectangles indicate domains of Mid1p sufficient for the role denoted below each rectangle.

Role of Mid1p in recruiting contractile ring proteins to nodes. IQGAP Rng2p is proposed to link Mid1p to Myo2 in nodes (Almonacid *et al.*, 2011; Laporte *et al.*, 2011; Padmanabhan *et al.*, 2011). The first four domains of Mid1p appear to provide these interactions, since cells depending on M1-14 accumulate Myo2 in nodes with M1-14 around the equator. Furthermore, construct Mid1p (1-580), just two residues longer than M1-14, interacts with Rng2p and myosin-II essential light chain Cdc4p in coimmunoprecipitation experiments (Lee and Wu, 2012). Association with Rng2p likely depends on domain M1-1, since a purified construct consisting of residues 1-100 of M1-1 binds a C-terminal fragment of Rng2p (Almonacid *et al.*, 2011). Domain M1-4 is not required, since construct M1-13 lacking domain M1-4 recruits Myo2 to nodes. Mid1p is believed to interact with Cdc12p indirectly via F-BAR protein Cdc15p in nodes (Carnahan and Gould, 2003; Laporte *et al.*, 2011). Construct Mid1p (1-580), just two residues longer than M1-14, interacts with F-BAR Cdc15p in coimmunoprecipitation experiments (Lee and Wu, 2012), and cells depending on M1-14 accumulate formin Cdc12p in nodes with M1-14. Nevertheless, we found that Cdc12p concentrates in nodes lacking Mid1p and Cdc15p (see accompanying article, Saha and Pollard, 2012), so other parallel interactions between node components and Cdc12p can substitute for Mid1p (Figure 8 in Saha and Pollard, 2012, indicates that these partners are unknown). Similarly, M1-14 is missing from some nodes with Blt1p, Myo2, and Cdc12p, indicating that nodes may have

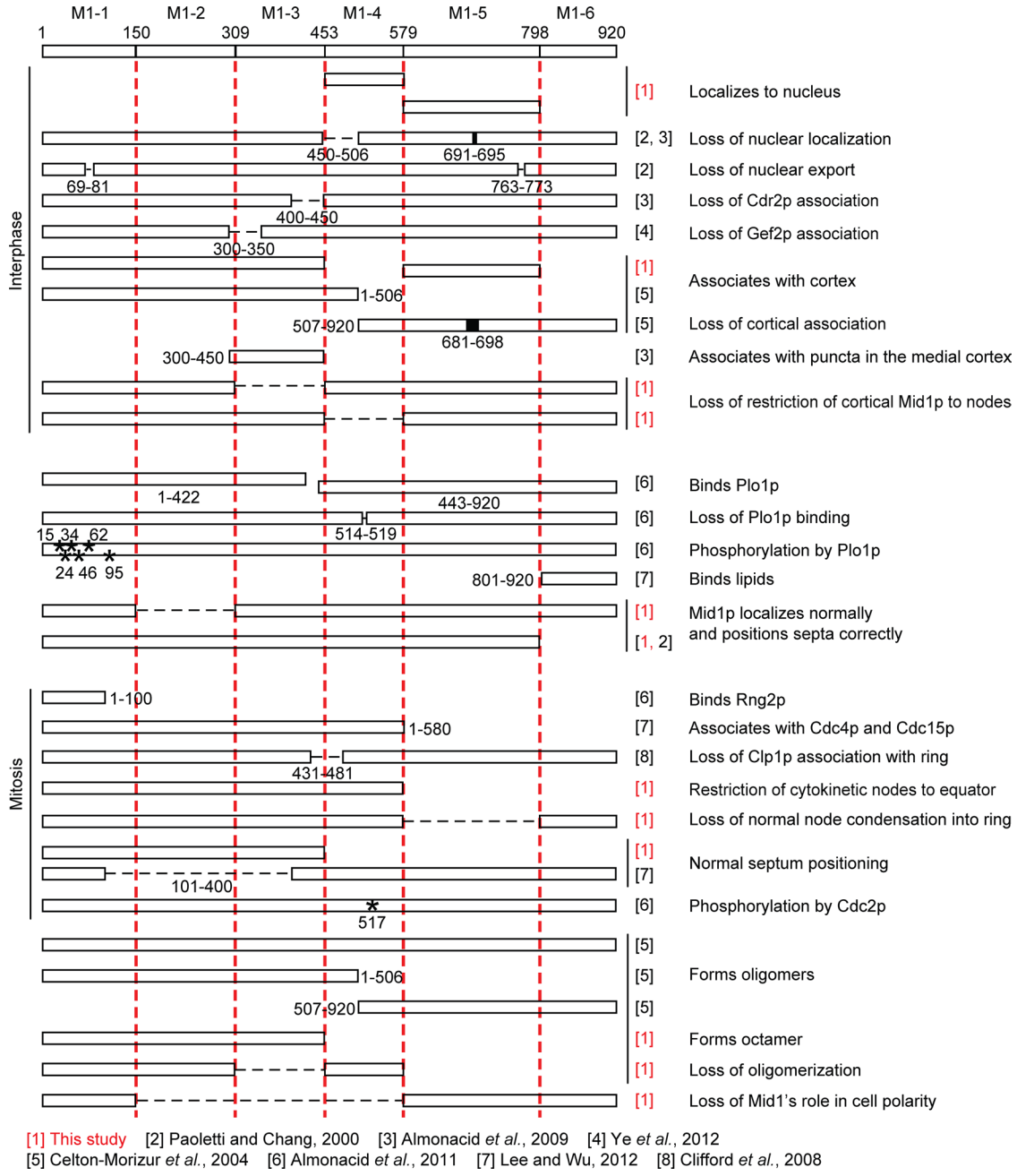

FIGURE 9: Summary of experiments on regions of Mid1p important for intracellular localization and function. The open bar at the top shows Mid1p and its six domains: M1-1 (residues 1–149), M1-2 (150–308), M1-3 (309–452), M1-4 (453–578), M1-5 (579–797), and M1-6 (798–920). The red broken lines represent domain boundaries. The open bars represent constructs of Mid1p sufficient for a particular role listed to the far right. Mutations (black bars) or deletions (broken lines) in these constructs result in weakening or total loss of activity. Stars represent phosphorylation sites. Vertical lines group multiple bars together. Vertical lines to the right, group of Mid1p constructs contributing to the same role; vertical lines to the left, group of Mid1p constructs with roles either in interphase or mitosis. Mid1p constructs between the groups representing interphase and mitosis function in both of these cell cycle stages. Precise timing is unclear for rest of the constructs. Boundary residues are listed to the side of or below the open bars, black bars, broken lines, and phosphorylation sites. The numbers in square brackets to the right of each bar give the references to the work on each Mid1p construct cited at the bottom of the figure.

binding sites for these proteins in addition to Rng2p, Cdc15p, and Mid1p.

Role of Mid1p in contractile ring formation by node condensation. Insoluble domain M1-5 is not required to place nodes and rings close to the equator, but cells depending on Mid1p constructs without M1-5 do not condense nodes with clock-like precision into contractile rings. Instead, nodes transition into strands, and strands slowly form rings. If the nodes are restricted to the equator, as in cells depending on M1-14, they generate strands that

are also confined in a narrow zone around the equator. The spatial proximity among growing strands increases random encounters between strands, and this allow strands in ~90% cells to merge into rings with minimal defects in position or orientation. About 10% of cells depending on M1-14 fail to form a contractile ring (Figure 5L), probably because strands grow beyond the equatorial region spanning almost the entire length of the cell (Supplemental Video S1). The time required for strands to close into a ring in M1-14 cells varies more than the time for nodes to condense into rings in wild-type cells, and these rings begin to constrict without the normal ~25-min maturation period after ring formation.

More work is required to understand how domain M1-5 contributes to the normal node condensation mechanism. The cortex-binding activity of M1-5 may be important, because during early mitosis a Mid1p construct with mutations in a segment of the domain M1-5 implicated in association with the cortex (residues 681–698) localized to strands in the cortex (Celton-Morizur *et al.*, 2004). It remains to be tested whether and how the cortex-binding activity of M1-5 contributes to the normal pathway of node condensation.

MATERIALS AND METHODS

Bacterial expression screen

We used primer A, 5′ GACCAATGTCAGCTG**GGATCC**NNNNNN-NNNNNNNNN 3′, and primer B, 5′ GACCAATGTCAGCTG**GGATCC** 3′, for Taq DNA polymerase amplification of a library of Mid1 cDNA fragments using the two-step tagged random primer PCR (T-PCR) (Grothues *et al.*, 1993). In the first step, a 25-µl reaction containing 2.2 nM Mid1 cDNA, 100 nM primer A, and 0.2 mM of each deoxyribonucleotide triphosphate (dNTP) was heated at 94°C for 2 min, followed by two cycles of 94°C × 15 s, 42°C × 5 min, 72°C × 3 min 30 s, and a final step at 72°C × 10 min. PCR products were purified by spin column (Qiagen, Valencia, CA) to remove primer A and eluted into 30 µl of water. Primer B, 5 µM, along with 0.2 mM of each dNTP, was added to this in the second step, and a 50-µl reaction was heated at 94°C for 2 min, followed by 30 cycles of 94°C × 15 s, 33°C × 30 s, 72°C × 3 min 30 s, and a final step at 72°C × 10 min. The products from five reactions were run on 0.8% agarose gel, and fragments varying in size from ~200 base pairs to 2.8 kb (Mid1 cDNA length) were purified using a Gel Extraction Kit (Qiagen).

Jian-Qiu Wu (Ohio State University) cloned mEGFP cDNA into pQE80L vector between the *Bam*HI and *Sal*I sites to obtain the construct hexahistidine-mEGFP (JQW110). We cloned the linker sequence 5′ GCTAGCGAGAATCTTTATTTTCAGGGAAGT 3′ encoding the TEV protease cleavage site immediately 3′ to the *Bam*HI site in JQW110, using the QuikChange II Site-Directed Mutagenesis Kit (Stratagene, Santa Clara, CA), to obtain the plasmid vector pSSB3-4.

T-PCR products and pSSB3-4 were digested with *Bam*HI; the vector was treated with calf intestinal phosphatase, ligated using a Roche Rapid DNA Ligation Kit (Roche, Indianapolis, IN), transformed into Invitrogen One Shot TOP10 chemically competent cells (Invitrogen, Carlsbad, CA), and plated on LB plates containing 0.1 mg/ml ampicillin and 0.2 mM isopropyl-β-D-1-thiogalactopyranoside (IPTG). After incubation at 37°C for 18 h, followed by 24 h at 33°C, the plates were imaged with an ultraviolet (UV) transilluminator (TE-312S, 312-nm UV lamp; Slimline; Spectroline, Westbury, NY) using a Kodak DC290 camera (Kodak, Rochester, NY) with a Kodak F3.0-4.7 3× autofocus lens and a Marumi 49-mm +3 filter (Marumi Optical Co., Tokyo, Japan). The exposure time was 0.5 s.

Fluorescent colonies were tested for the presence of inserts using colony PCR, and plasmids from positive clones were retested for the presence of inserts using *Bam*HI digestion and agarose gel electrophoresis. Positive plasmids were sequenced using primer 5′ CGGATAACAATTTCACACAG 3′ to identify inserts of Mid1 cDNA fragment.

Strain construction

We modified tdTomato-kanMX6 (pFA6a) in a site-directed mutagenesis reaction using primers 5′ CGCTGCAGGTCGACATGGGATCCGCTAGCGAGAATCTTTATTTTCAGGGAAGTATGGTGAGCAAGGGC 3′ and 5′ GCCCTTGCTCACCATACTTCCCTGAAAATAAAGATTCTCGCTAGCGGATCCCATGTCGACCTGCAGCG 3′ to generate 5′ ATG-*Bam*HI site-TEV protease cleavage site-tdTomato-kanMX6 3′ (pSSB57). mEGFP was cloned into the *Xma*I site of pSSB3-4, and the resulting 2mEGFP cassette was used to replace tdTomato in pSSB57-3 between the *Nhe*I and *Asc*I sites (pSSB66). pFA6a clones of constructs M1-1-2mEGFP, M1-2-2mEGFP, M1-3-2mEGFP, M1-4-2mEGFP, M1-Δ1-2mEGFP, and M1-Δ6-2mEGFP were generated by cloning Mid1p (1–149), Mid1p (150–308), Mid1p (309–452), Mid1p (453–578), Mid1p (150–920), and Mid1p (1–797), respectively, into the *Bam*HI site of pSSB66. We generated pFA6a clone of construct M1-Δ2-2mEGFP by cloning Mid1p (1–149) into the *Bam*HI site and Mid1p (309–920) into the *Nhe*I site of pSSB66, respectively. pFA6a clones of M1-14-tdTomato and M1-12-tdTomato were generated by cloning Mid1p (1–578) and Mid1p (1–308) into the *Bam*HI site of pSSB57. We PCR amplified M1-1-2mEGFP, M1-2-2mEGFP, M1-3-2mEGFP, M1-4-2mEGFP, M1-Δ1-2mEGFP, M1-Δ2-2mEGFP, M1-Δ6-2mEGFP, M1-14-tdTomato, and M1-12-tdTomato integration cassettes from pFA6a clones using primers 5′ TGCTTATATGATACTGTGTCCACATTTTAACACTCGATAAGGTATTATAGTCTGTAAAGTCTAATTAAGCTATCCTGACGTGCAGGTCGACATGGGATCC 3′ and 5′ ACTCCCTCATTTAGTAAATCCGATAAGTAAAAATTATTCAAAAAATACATTAAGACGATTAGTATTCATAAATTCAGATAGAATTCGAGCTCGTTTAAAC 3′ and integrated the cassettes into the *mid1* locus in SSP40-12 (Δ*mid1* strain), generating SSP58-5, SSP59-3, SSP64-4, SSP60-3, SSP53-2, SSP54-3, SSP56-4, SSP45-6, and SSP44-3, respectively (Table 2). We generated SSP80-1 by inserting the nuclear export sequence Mid1p (69–81) immediately 5′ to the upstream *Bam*HI site in the pFA6a clone of M1-Δ1-2mEGFP and integrating the resulting construct into the *mid1* locus in SSP40-12 (Table 2).

We inserted 626 base pairs of Mid1 5′ untranslated region between the *Kpn*I and *Xho*I sites and cloned M1-Δ3-mEGFP, M1-Δ4-mEGFP, M1-Δ5-mEGFP, and M1-13-mEGFP between the *Xho*I and *Not*I sites of pJK148. The resulting pJK148 constructs were linearized by *Nru*I digestion and integrated into the *leu1* locus of SSP40-12, generating SSP75-1, SSP74-2, SSP76-1, and SSP117-1 respectively. SSP19-3 and SSP20-6 were generated identically from a pKJ148 construct that contained a *3xnmt1* promoter cloned between the *Kpn*I and *Xho*I sites and respectively Mid1p (579-797)-tdTomato and Mid1p (798-920)-tdTomato engineered between the *Xho*I and *Not*I sites.

Microscopy and image analysis

Microscopy and image analysis were performed as in Saha and Pollard (2012).

Expression and purification of Mid1p fragments

S. pombe DNA sequence coding for M1-1 (Mid1p amino acid residues 1–149), M1-2 (residues 150–308), M1-3 (residues 309–452), M1-4 (residues 453–578), M1-5 (residues 579–797), M1-6 (residues 798–920), M1-14 (residues 1–578), M1-13 (residues 1–452), and M1-12 (residues 1–308) were cloned into the *Bam*HI site of pQE80L vector. A construct coding for M1-124 (residues 1–308-GSACELGT-453–578) was generated by cloning both

Strain	Genotype	Source	Strain	Genotype	Source
SSP1-3	*h+ mid1-mEGFP-kanMX6 leu1-32 ura4-D18 his3-D1 ade6-M210*	This study	SSP59-3	*h+ M1-2-2mEGFP-kanMX6 leu1-32 ura4-D18 his3-D1 ade6-M210*	This study
SSP2-3	*h+ Δmid1::kanMX6 leu1-32 ura4-D18 his3-D1 ade6-M210*	This study	SSP60-3	*h+ M1-4-2mEGFP-kanMX6 leu1-32 ura4-D18 his3-D1 ade6-M210*	This study
SSP19-3	*h+ Δmid1::kanMX6 leu1-32::P3xnmt1-M1-5-tdTomato-leu1+ ura4-D18 his3-D1 ade6-M210*	This study	SSP64-4	*h+ M1-3-2mEGFP-kanMX6 leu1-32 ura4-D18 his3-D1 ade6-M210*	This study
SSP20-6	*h+ Δmid1::kanMX6 leu1-32::P3xnmt1-M1-6-tdTomato-leu1+ ura4-D18 his3-D1 ade6-M210*	This study	SSP73-4	*blt1-mEGFP-kanMX6 M1-14-tdTomato-kanMX6 leu1-32 ura4-D18*	This study
SSP40-12	*h+ Δmid1::natMX6 leu1-32 ura4-D18 his3-D1 ade6-M210*	This study	SSP74-2	*h+ Δmid1::natMX6 leu1-32::Pmid1-M1-Δ4-mEGFP-leu1+ ura4-D18 his3-D1 ade6-M210*	This study
SSP44-3	*h+ M1-12-tdTomato-kanMX6 leu1-32 ura4-D18 his3-D1 ade6-M210*	This study	SSP75-1	*h+ Δmid1::natMX6 leu1-32::Pmid1-M1-Δ3-mEGFP-leu1+ ura4-D18 his3-D1 ade6-M210*	This study
SSP45-6	*h+ M1-14-tdTomato-kanMX6 leu1-32 ura4-D18 his3-D1 ade6-M210*	This study	SSP76-1	*h+ Δmid1::natMX6 leu1-32::Pmid1-M1-Δ5-mEGFP-leu1+ ura4-D18 his3-D1 ade6-M210*	This study
SSP48-1	*h+ tea1-mEGFP-kanMX6 leu1-32 ura4-D18 his3-D1 ade6-M210*	This study	SSP80-1	*h+ NES-M1-Δ1-2mEGFP-kanMX6 leu1-32 ura4-D18 his3-D1 ade6-M210*	This study
SSP49-1	*h+ tea1-mEGFP-kanMX6 Δmid1::natMX6 leu1-32 ura4-D18 his3-D1 ade6-M210*	This study	SSP81-1	*tea1-mEGFP-kanMX6 M1-Δ1-tdTomato-kanMX6 leu1-32 ura4-D18 his3-D1 ade6-M210*	This study
SSP50-3	*h+ tea1-mEGFP-natMX6 M1-14-tdTomato-kanMX6 leu1-32 ura4-D18 his3-D1 ade6-M210*	This study	SSP112-5	*cdc12-3GFP-kanMX6 M1-14-tdTomato-kanMX6 leu1-32 ura4-D18 his3-D1*	This study
SSP51-1	*h+ rlc1-3GFP-kanMX6 M1-14-tdTomato-kanMX6 leu1-32 ura4-D18 ade6-M210*	This study	SSP113-7	*blt1-mEGFP-kanMX6 M1-14-tdTomato-kanMX6 sad1-mRFP1-kanMX6 leu1-32 ura4-D18*	This study
SSP53-2	*h+ M1-Δ1-2mEGFP-kanMX6 leu1-32 ura4-D18 his3-D1 ade6-M210*	This study	SSP114-5	*rlc1-3GFP-kanMX6 M1-14-tdTomato-kanMX6 sad1-mEGFP-kanMX6 leu1-32 ura4-D18 ade6-M210*	This study
SSP54-3	*h+ M1-Δ2-2mEGFP-kanMX6 leu1-32 ura4-D18 his3-D1 ade6-M210*	This study	SSP117-1	*h+ Δmid1::natMX6 leu1-32::Pmid1-M1-13-mEGFP-leu1+ rlc1-mCherry-natMX6 ura4-D18 his3-D1 ade6-M210*	This study
SSP56-4	*h+ M1-Δ6-2mEGFP-kanMX6 leu1-32 ura4-D18 his3-D1 ade6-M210*	This study			
SSP58-5	*h+ M1-1-2mEGFP-kanMX6 leu1-32 ura4-D18 his3-D1 ade6-M210*	This study			

TABLE 2: *S. pombe* strains used in this study.

M1-12 (residues 1–308) into the *Bam*HI site and M1-4 (residues 453–578) into the *Kpn*I site of pQE80L vector. These clones were transformed into ArcticExpress cells (Stratagene). Overnight saturated culture of these cells were diluted 1:100 times into LB medium containing 0.1 mg/ml ampicillin and 0.02 mg/ml gentamicin, grown for 5–6 h at 25°C, induced using 1 mM IPTG, and grown overnight at 10°C. The cells from every 1-l culture were harvested, resuspended in ~10 ml of lysis buffer (50 mM sodium phosphate, 300 mM NaCl, 10 mM imidazole, pH 8.0), and lysed using sonication. Every 50 ml of lysis buffer also contained one protease inhibitor cocktail tablet (Roche), 7.8 mg of benzamidine HCl, and 1 mM phenylmethanesulfonyl fluoride. Cell lysate was separated into pellet and supernatant fractions by centrifugation at 18,000 rpm for 45 min using a Beckman JA-30.50 Ti rotor (Beckman Coulter, Brea, CA). M1-5 was predominantly found in the pellet. Other Mid1p fragments were purified from the supernatant as follows.

List of buffers used: buffer A (50 mM sodium phosphate, 300 mM NaCl, pH 8.0), buffer B (50 mM sodium phosphate, 300 mM NaCl, 1 mM dithiothreitol [DTT], 0.5 mM EDTA, 6 M urea [Fluka 02493], pH 8.0), buffer C (20 mM bis-Tris, 50 mM NaCl, 6 M urea, 1 mM DTT, 0.5 mM EDTA), buffer D (50 mM sodium phosphate, 300 mM NaCl, 1 mM DTT, 0.5 mM EDTA, pH 8.0), buffer E (20 mM Tris, 50 mM NaCl, 1 mM DTT, pH 8.0), buffer F (20 mM Tris, 1 M NaCl, 1 mM DTT, pH 8.0), and buffer G (10 mM Tris, 150 mM NaCl, 1 mM Tris(2-carboxyethyl)phosphine hydrochloride [TCEP], pH 8.0).

M1-1 and M1-3 (from 1 l of bacterial culture)

Step 1. Ni-NTA affinity purification. Samples were purified on Ni-NTA agarose resin (Qiagen) in buffer A. Samples were loaded onto a 1-ml column in buffer A with 10 mM imidazole, pH 8.0. The column was washed with ~25 ml of buffer A with 20 mM

imidazole, pH 8.0, and the protein was eluted with buffer A containing 250 mM imidazole, pH 8.0.

Step 2. Dialysis. The sample was dialyzed for ~16 h at 4°C into buffer B.

Step 3. Ni-NTA affinity purification in 6 M urea. The sample was loaded onto a 1-ml column of Ni-NTA agarose resin (Qiagen) in buffer B. The column was washed with ~25 ml of buffer B containing 20 mM imidazole, pH 8.0, and eluted with buffer B containing 250 mM imidazole, pH 8.0.

Step 4. Dialysis. The sample was dialyzed for ~16 h at 4°C into buffer C (at pH 6.4 for M1-1 or pH 7.3 for M1-3).

Step 5. Anion exchange chromatography. The sample was loaded onto a 0.9-ml column of Q-Sepharose resin (GE Healthcare, Piscataway, NJ) in buffer C. M1-1 and M1-3 eluted in flowthrough and were refolded by dialysis for ~16 h at 4°C into buffer D.

M1-2, M1-4, and M1-6 (from 1 l of bacterial culture)

Step 1. Ni-NTA affinity purification. Samples were purified on a 1-ml column of Ni-NTA agarose resin (Qiagen) in buffer A with 10, 20, and 250 mM imidazole, pH 8.0, during loading, washing, and elution. Approximately 25 ml of buffer was used for washing.

Step 2. Size exclusion chromatography. Eluent from the Ni-NTA column was concentrated to ~0.4 ml in an Amicon Ultra 5000 MWCO centrifugal filter (Millipore, Billerica, MA) and purified on a 24-ml column of Superdex 200 (Pharmacia Biotech, GE Healthcare) in buffer A.

Constructs M1-14, M1-13, M1-12, and M1-124. These were purified in a sequence of three purification steps: Ni-NTA affinity, anion-exchange, and size-exclusion chromatography as follows.

M1-14 (from 8 l of bacterial culture)

Step 1. Ni-NTA affinity purification. Samples were purified on Ni-NTA agarose resin (Qiagen) in buffer A. Samples were loaded onto an 8-ml column in buffer A with 10 mM imidazole, pH 8.0. The column was washed with ~100 ml of buffer A with 20 mM imidazole, pH 8.0, and the protein was eluted with buffer A containing 250 mM imidazole pH 8.0.

Step 2. Dialysis. Samples were dialyzed for ~16 h at 4°C into buffer E.

Step 3. Anion exchange chromatography. Samples were loaded onto a 6-ml column of Q-Sepharose resin (GE Healthcare) in buffer E. The column was washed with ~100 ml of 150 mM NaCl in 20 mM Tris, pH 8.0, and eluted with 1 M NaCl in 20 mM Tris, pH 8.0.

Step 4. Size exclusion chromatography. Eluent from the Q-Sepharose column was concentrated to ~1 ml in an Amicon Ultra 10,000 MWCO centrifugal filter and purified on a 120-ml column of Superdex 200 (GE Healthcare) in 20 mM Tris, 1 M NaCl, pH 8.0.

M1-13 (from 8 l of bacterial culture)

Step 1. Ni-NTA affinity purification. Samples were purified on Ni-NTA agarose resin (Qiagen) in buffer A. Samples were loaded onto an 8-ml column in buffer A with 10 mM imidazole, pH 8.0. The column was washed with ~150 ml of buffer A with 20 mM imidazole, pH 8.0, and the protein was eluted with buffer A containing 250 mM imidazole pH 8.0.

Step 2. Dialysis. Samples were dialyzed for ~16 h at 4°C into buffer E.

Step 3. Anion exchange chromatography. Samples were loaded onto an 8-ml column of Mono Q 10/100 GL (GE Healthcare) in buffer E and washed with 1 column volume of buffer E to wash out unbound proteins. This was followed by collection of 2-ml fractions during a linear salt gradient from 10 to 37% buffer F over 24 column volumes at 0.75 ml/min. M1-13 eluted within the peak at 19–22% buffer F.

Step 4. Size exclusion chromatography. The early peak fractions from step 3 (fractions 30–35) containing M1-13 were pooled and concentrated to <2 ml using an Amicon Ultra 10000 MWCO centrifugal filter and purified on a 120-ml column of Superdex 200 (GE Healthcare) in buffer G.

M1-12 (from 4 l of bacterial culture)

Step 1. Ni-NTA affinity purification. Samples were purified on Ni-NTA agarose resin (Qiagen) in buffer A. Samples were loaded onto a 4-ml column in buffer A with 10 mM imidazole, pH 8.0. The column was washed with ~100 ml of buffer A with 20 mM imidazole, pH 8.0, and the protein was eluted with buffer A containing 250 mM imidazole, pH 8.0.

Step 2. Dialysis. Samples were dialyzed for ~16 h at 4°C into buffer E.

Step 3. Anion exchange chromatography. Samples were loaded onto an 8-ml column of Mono Q 10/100 GL (GE Healthcare) in buffer E and washed with one column volume of buffer E to wash out unbound proteins. This was followed by collection of 2-ml fractions during a linear salt gradient from 10 to 25% buffer F over seven column volumes at 0.75 ml/min. M1-12 eluted within the peak at 13–16% buffer F.

Step 4. Size exclusion chromatography. The peak fractions from step 3 containing M1-12 were pooled and concentrated to <2 ml using an Amicon Ultra 10000 MWCO centrifugal filter and purified on a 120-ml column of Superdex 200 (GE Healthcare) in buffer G.

M1-124 (from 8 l of bacterial culture)

Step 1. Ni-NTA affinity purification. Samples were purified on Ni-NTA agarose resin (Qiagen) in buffer A. Samples were loaded onto an 8-ml column in buffer A with 10 mM imidazole, pH 8.0. The column was washed with ~175 ml of buffer A with 20 mM imidazole, pH 8.0, and the protein was eluted with buffer A containing 250 mM imidazole, pH 8.0.

Step 2: Dialysis. Samples were dialyzed for ~16 h at 4°C into buffer E.

Step 3. Anion exchange chromatography. Samples were loaded onto an 8-ml column of Mono Q 10/100 GL (GE Healthcare) in buffer E and washed with 1 column volume of buffer E to wash out unbound proteins. This was followed by collection of 2-ml fractions during a linear salt gradient from 10 to 37% buffer F over 24 column volumes at 0.25 ml/min. M1-124 eluted within the peak at 14.7–16.6% buffer F.

Step 4. Size exclusion chromatography. The peak fractions from step 3 (fractions 17–23) containing M1-124 were pooled and concentrated to <2 ml using an Amicon Ultra 10000 MWCO centrifugal filter and purified on a 120-ml column of Superdex 200 (GE Healthcare) in buffer G.

Spectroscopy

Circular dichroism spectra for Mid1p fragments were collected with Jasco (Jasco, Tokyo, Japan) and Aviv (Aviv Biomedical, Lakewood, NJ) CD spectrophotometers, and fluorescence emission scans were obtained with a AlphaScan fluorimeter (PTI, Birmingham, NJ).

Sedimentation velocity analytical ultracentrifugation

Sedimentation velocity experiments were performed at 20°C with a Beckman XL-I analytical ultracentrifuge. Samples were clarified by centrifugation at 14,000 rpm for 5–10 min in a tabletop centrifuge, and ~400 µl of samples were loaded in two-channel centerpieces fitted with quartz windows in a four-hole rotor. During centrifugation at 42,000, 35,000, or 28,000 rpm samples were monitored by scanning absorbance at 280 nm versus radial location every 4–5 min. SEDFIT software was used to analyze the sedimentation profiles, and SEDNTERP software was used to calculate the density and viscosity of buffers from their compositions and the partial specific volume of the proteins from their amino acid composition.

ACKNOWLEDGMENTS

We thank J. B. Moseley, J.-Q. Wu, and D. R. Kovar for strains; I. C. Berke and members of D. M. Engelman's lab for help with ultracentrifugation experiments; members of L. Regan's lab and A. Schepartz's lab for help with CD spectroscopy; M. J. Solomon and Y.-L. Wang for helpful suggestions on the text and organization of the manuscript; and members of our lab for helpful discussions. This work was supported by National Institutes of Health Research Grant GM-026132 to T.D.P. and an Edward L. Tatum Fellowship to S.S. S.S. dedicates this work to his sister, Shreyasee Saha.

REFERENCES

Almonacid M, Celton-Morizur S, Jakubowski JL, Dingli F, Loew D, Mayeux A, Chen JS, Gould KL, Clifford DM, Paoletti A (2011). Temporal control of contractile ring assembly by Plo1 regulation of myosin II recruitment by Mid1/anillin. Curr Biol 21, 473–479.

Almonacid M, Moseley JB, Janvore J, Mayeux A, Fraisier V, Nurse P, Paoletti A (2009). Spatial control of cytokinesis by Cdr2 kinase and Mid1/anillin nuclear export. Curr Biol 19, 961–966.

Carnahan RH, Gould KL (2003). The PCH family protein, Cdc15p, recruits two F-actin nucleation pathways to coordinate cytokinetic actin ring formation in *Schizosaccharomyces pombe*. J Cell Biol 162, 851–862.

Celton-Morizur S, Bordes N, Fraisier V, Tran PT, Paoletti A (2004). C-terminal anchoring of mid1p to membranes stabilizes cytokinetic ring position in early mitosis in fission yeast. Mol Cell Biol 24, 10621–10635.

Chang F, Woollard A, Nurse P (1996). Isolation and characterization of fission yeast mutants defective in the assembly and placement of the contractile actin ring. J Cell Sci 109, 131–142.

Clifford DM, Wolfe BA, Roberts-Galbraith RH, McDonald WH, Yates JR 3rd, Gould KL (2008). The Clp1/Cdc14 phosphatase contributes to the robustness of cytokinesis by association with anillin-related Mid1. J Cell Biol 181, 79–88.

Grothues D, Cantor CR, Smith CL (1993). PCR amplification of megabase DNA with tagged random primers (T-PCR). Nucleic Acids Res 21, 1321–1322.

Hachet O, Simanis V (2008). Mid1p/anillin and the septation initiation network orchestrate contractile ring assembly for cytokinesis. Genes Dev 22, 3205–3216.

Huang Y, Yan H, Balasubramanian MK (2008). Assembly of normal actomyosin rings in the absence of Mid1p and cortical nodes in fission yeast. J Cell Biol 183, 979–988.

Jacobs SA, Podell ER, Wuttke DS, Cech TR (2005). Soluble domains of telomerase reverse transcriptase identified by high-throughput screening. Protein Sci 14, 2051–2058.

Kawasaki M, Inagaki F (2001). Random PCR-based screening for soluble domains using green fluorescent protein. Biochem Biophys Res Commun 280, 842–844.

Kovar DR, Kuhn JR, Tichy AL, Pollard TD (2003). The fission yeast cytokinesis formin Cdc12p is a barbed end actin filament capping protein gated by profilin. J Cell Biol 161, 875–887.

Laporte D, Coffman VC, Lee IJ, Wu JQ (2011). Assembly and architecture of precursor nodes during fission yeast cytokinesis. J Cell Biol 192, 1005–1021.

Lebowitz J, Lewis MS, Schuck P (2002). Modern analytical ultracentrifugation in protein science: a tutorial review. Protein Sci 11, 2067–2079.

Lee IJ, Wu JQ (2012). Characterization of Mid1 domains for targeting and scaffolding in fission yeast cytokinesis. J Cell Sci 125, 2973–2985.

Marsden RL, McGuffin LJ, Jones DT (2002). Rapid protein domain assignment from amino acid sequence using predicted secondary structure. Protein Sci 11, 2814–2824.

Martin SG, Berthelot-Grosjean M (2009). Polar gradients of the DYRK-family kinase Pom1 couple cell length with the cell cycle. Nature 459, 852–856.

Morrell JL, Nichols CB, Gould KL (2004). The GIN4 family kinase, Cdr2p, acts independently of septins in fission yeast. J Cell Sci 117, 5293–5302.

Moseley JB, Mayeux A, Paoletti A, Nurse P (2009). A spatial gradient coordinates cell size and mitotic entry in fission yeast. Nature 459, 857–860.

Motegi F, Mishra M, Balasubramanian MK, Mabuchi I (2004). Myosin-II reorganization during mitosis is controlled temporally by its dephosphorylation and spatially by Mid1 in fission yeast. J Cell Biol 165, 685–695.

Padmanabhan A, Bakka K, Sevugan M, Naqvi NI, D'Souza V, Tang X, Mishra M, Balasubramanian MK (2011). IQGAP-related Rng2p organizes cortical nodes and ensures position of cell division in fission yeast. Curr Biol 21, 467–472.

Paoletti A, Chang F (2000). Analysis of mid1p, a protein required for placement of the cell division site, reveals a link between the nucleus and the cell surface in fission yeast. Mol Biol Cell 11, 2757–2773.

Pollard TD, Wu JQ (2010). Understanding cytokinesis: lessons from fission yeast. Nat Rev Mol Cell Biol 11, 149–155.

Saha S, Pollard TD (2012). Anillin-related protein Mid1p coordinates the assembly of the cytokinetic contractile ring in fission yeast. Mol Biol Cell 23, 3982–3992.

Sohrmann M, Fankhauser C, Brodbeck C, Simanis V (1996). The dmf1/mid1 gene is essential for correct positioning of the division septum in fission yeast. Genes Dev 10, 2707–2719.

Vavylonis D, Wu JQ, Hao S, O'Shaughnessy B, Pollard TD (2008). Assembly mechanism of the contractile ring for cytokinesis by fission yeast. Science 319, 97–100.

Waldo GS, Standish BM, Berendzen J, Terwilliger TC (1999). Rapid protein-folding assay using green fluorescent protein. Nat Biotechnol 17, 691–695.

Wu JQ, Kuhn JR, Kovar DR, Pollard TD (2003). Spatial and temporal pathway for assembly and constriction of the contractile ring in fission yeast cytokinesis. Dev Cell 5, 723–734.

Wu JQ, Pollard TD (2005). Counting cytokinesis proteins globally and locally in fission yeast. Science 310, 310–314.

Wu JQ, Sirotkin V, Kovar DR, Lord M, Beltzner CC, Kuhn JR, Pollard TD (2006). Assembly of the cytokinetic contractile ring from a broad band of nodes in fission yeast. J Cell Biol 174, 391–402.

Ye Y, Lee IJ, Runge KW, Wu JQ (2012). Roles of putative Rho-GEF Gef2 in division-site positioning and contractile-ring function in fission yeast cytokinesis. Mol Biol Cell 23, 1181–1195.